



Evaluation of powder mixing homogeneity for laser-directed energy deposition (L-DED) of functionally graded materials

Bo Xin¹ · Yuting Wang¹ · Wenfu Zhu² · Jiaxin Qin¹ · Gang Cao¹

Received: 28 May 2024 / Accepted: 6 September 2024

© The Author(s), under exclusive licence to Springer-Verlag London Ltd., part of Springer Nature 2024

Abstract

Improving the mixing homogeneity of heterogeneous powder in real time plays an essential role in ensuring the forming quality of functionally graded materials (FGM) produced by laser-directed energy deposition (L-DED). In order to achieve a high performance of material composition and proportion control as forming FGM parts, this paper investigates the mixing mechanism of several typical powders including 316L and NiCrCoAlY used for the L-DED process driven by compressed gas. An innovative pneumatic powder mixer is designed and optimized by the CFD-DEM simulation method to analyze the mixing characteristics of heterogeneous particles. To improve the real-time mixing homogeneity of different mixing ratios in the conveying process, mixing experiments based on differences in powder properties were conducted by the additive-subtractive composite machining center, and a coefficient of variation method was proposed to describe the mixing homogeneity of non-uniform powders. The results of micro-morphology and EDS indicate that the mixing quality of the two-phase flow is significantly enhanced with the four 45° compression inlets and 2 m/s inlet velocity structure. The results show that the numerical analysis method proposed in this paper can effectively describe the mixing law of heterogeneous particles, and the compressed air intake velocity should not exceed the initial two-phase flow velocity. The horizontal and vertical components generated by the compressed air intake at 45° are more conducive to the formation of favorable perturbations to the two-phase flow, and the number of four and eight compressed air intakes that act uniformly on the flow field is more appropriate. After a certain period of time, the two-phase flow with low error of mixed powder quality can be produced continuously. The mixed powder quality is obviously improved after the disturbance of compressed air intake. The mixing uniformity of powder with low spherical particle proportion can be effectively improved by increasing the preset mixing proportion of non-spherical particles.

Keywords Laser-directed energy deposition (L-DED) · Powder mixing · Gas-solid two-phase flow · Homogeneity · CFD-DEM simulation

1 Introduction

Functionally graded materials (FGM) are advanced composites composed of two or more materials with different ingredients or structures that change gradually [1]. With the help of FGM, a single part can have various physical or chemical properties, making it highly suitable for applications in aeronautics and astronautics, such as TiAl-based FGM

turbine blades and ceramic-based thermal protection fairings. Laser-directed energy deposition (L-DED) technology has been widely used for the rapid manufacturing of FGM parts, as well as similar metal matrix composites (MMC). The technical advantages of L-DED for FGM manufacturing include high automation and cladding speed [2], as well as greater flexibility in powder feeding and mixing for different materials. As shown in Fig. 1, the material composition and proportion of FGM formed by coaxial powder-feeding laser cladding can be conveniently and continuously controlled in real-time. However, there are also new challenges of powder feeding and mixing for L-DED. Fast and uniform mixing of heterogeneous powders before they are transported to the molten pool is the premise of forming FGM parts with accurate composition and preventing common defects

✉ Bo Xin
xinbo@me.neu.edu.cn

¹ School of Mechanical Engineering and Automation, Northeastern University, Shenyang 110819, China

² Shenyang Aircraft Industry (Group) Co., Ltd, Shenyang 110000, China

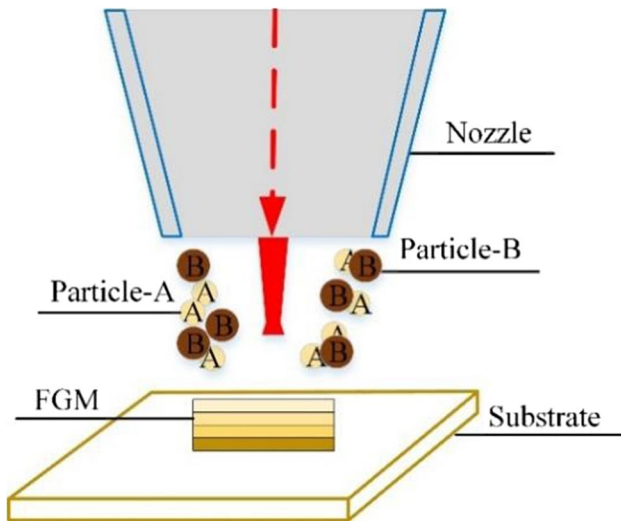


Fig. 1 Coaxial L-DED schematic diagram of functionally graded materials (FGM)

including local segregation, agglomeration [3], and harmful phase interfaces.

To address these challenges, multi-type powder mixing techniques have been well-suited. The mixing mechanism is mainly concluded as convection, shear, and diffusion [4]. Concretely, convection mixing can be interpreted as particle movement in a wide range of positions and contributes to the formation of circular flow in a container. Shear mixing is caused by the momentum exchange between particles with different velocities, which primarily occurs at the outlet position of powder mixers [1]. Diffusion mixing mainly occurs among particles in close proximity to each other. The powder feeding and mixing during the L-DED process is essentially a complex gas–solid two-phase flow consisting of particles in the solid phase and compressed gas. The volume fraction of particles in the two-phase flow is generally less than 10%, thus the two-phase flow belongs to a typical sparse flow and the powder mixing is mainly driven by convection and shear effects. Diffusion mixing has a modest effect and can be neglected. To thoroughly investigate the convection and shear effect in different types of powder mixers, lots of scholars have researched on numerical simulation of gas–solid two-phase flow. At present, the simulation methods mainly include the two-fluid model (TFM) [6, 7] methods based on the Eulerian–Eulerian framework [5] and multiphase particle-in-cell (MP-PIC) [8, 9], CFD-DEM [10, 11] methods based on the Eulerian–Lagrangian framework. In particular, the CFD-DEM method is widely adopted to capture the particle collision information and improve the credibility of the gas–solid two-phase flow simulation. For instance, Zhang [12], Varas [13], and Peng et al. [14] analyzed the interaction of gas–solid two-phase flow and simulated the particle motion properties by CFD-DEM. Sahan

et al. [15] found that the distribution of particles along the channel length and height can reflect the actual distribution of particles by the discrete element method (DEM). Paul [16] used DEM to study the mixing performance of mixers with different morphologies and found that non-spherical particles have poor fluidity, leading to poor mixing homogeneity. In addition, some research has investigated the homogenization and refinement of particles, as well as the mass and heat transfer of gas–solid two-phase flow based on CFD-DEM simulation [17, 18]. The previous research mostly focused on the simulation and analysis of dense-phase flow in mechanical powder mixers [19–21], with the aim of improving the mixing homogeneity. There has been considerable exploration of existing research on the flow and mixing characteristics of complex gas–solid two-phase flows. However, mechanical powder mixers do not meet the efficiency requirements for rapid powder mixing in the formation of FGM parts by L-DED. The powder mixing characteristics driven by compressed gas in sparse flow have been rarely investigated.

Based on the above analysis, the coupled CFD-DEM simulation approach is applicable to analyzing the motion and collision properties of heterogeneous particles in gas–solid two-phase flow. Thus, this article focuses on the mixing mechanism of heterogeneous powders in the L-DED process of metal functional gradient materials. CFD-DEM simulation was used to investigate the powder mixing characteristics and delve into the influence of particle size, density, and morphology on the mixing uniformity. Moreover, a set of L-DED FGM specimens was formed to further explore the effect of powder mixing uniformity on the micro-morphology.

2 Experimental scheme design

2.1 Experimental and test equipment

The powder mixing and L-DED forming experiments in this research were conducted at the SVW80C-3D additive and subtractive composite machining center, as shown in Fig. 2. The powder feeding and mixing system is composed of a nitrogen generator, air compressor, powder feeder, and mixer. Compressed nitrogen is produced by the DM-80 pressure swing adsorption (PSA) nitrogen generator and the ET-80 piston compressor for conveying powder and shielding gas.

The RC-PGF-D-2 negative pressure powder feeder with double silos (volumetric capacity, 1.1 L per silo) is connected to the gas outlet of the nitrogen generator and the inlet of the powder mixer. The valid range of particle size is 15 ~ 200 μm . According to the density of the mixing powder (316L and NiCrCoAlY powder) and the flow regulation

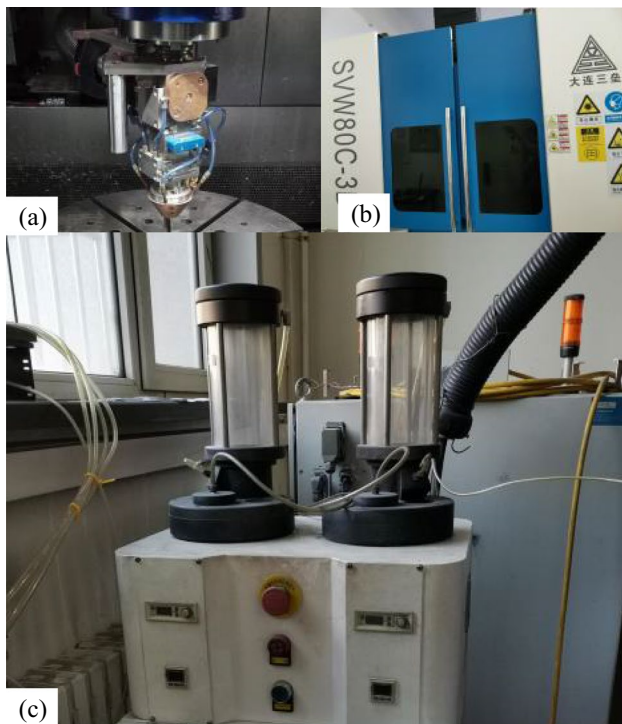


Fig. 2 SVW80C-3D additive and subtractive composite machining center: **a** laser deposition nozzle, **b** five-axis machining center, and **c** double cans powder feeder

range (1 ~ 20 L/min) of the RC-PGF-D-2 powder feeder, it can be calculated that the powder feed rate should be controlled within the range of 5 ~ 200 g/min, and the maximum error should be less than 5%.

Two different powders can be simultaneously transported at the same or different speeds from the double silos. To achieve rapid mixing of heterogeneous particles, an innovative pneumatic powder mixer was designed and its structure is shown in Fig. 3. The operating principle of the powder mixer is as follows: firstly, heterogeneous powders are transported from the negative pressure powder feeder and then flow into the powder mixer through the intake. Subsequently, the two-phase flow of heterogeneous powders is diverted by the splitter plate and then accumulates in the convection chamber through the conflux plate. Similar to a mechanical blender, the splitter and conflux plates can increase the convection mixing of the two-phase flow in the mixer and reduce the influence of gravity on the powders. When the two-phase flow enters the convection chamber, compressed gas simultaneously enters the convection chamber from the inlet at the bottom of the powder mixer in order to increase the convection mixing process.

Finally, the mixed powders are ejected from the outlet of the powder mixer and flow into the laser cladding head through the feeding pipes. The transparent mixing tank is made of polymethyl methacrylate (PMMA) so that the

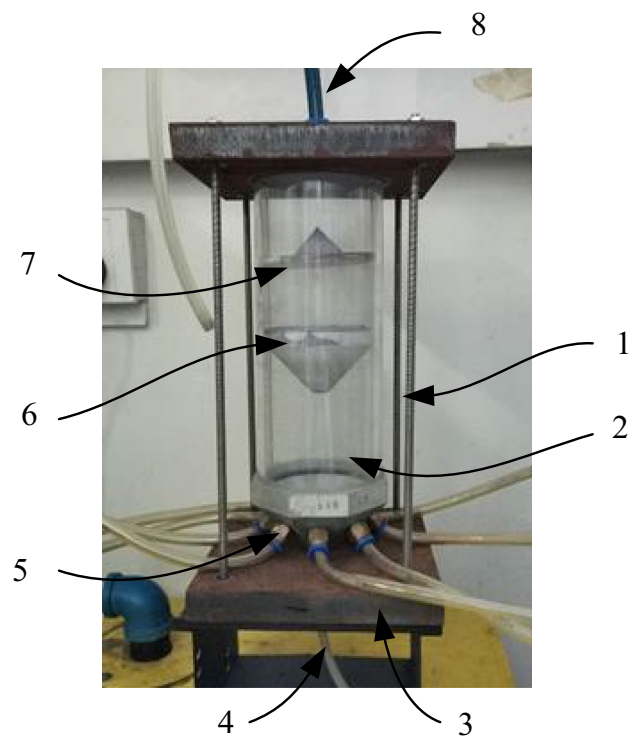


Fig. 3 Structure of pneumatic powder mixer: 1, mixing tank; 2, convection chamber; 3, fixed base; 4, powder outlet; 5, compression inlet; 6, conflux plate; 7, splitter plate; and 8, inlet

powders' motion trajectory can be conveniently observed. In addition, laser-cladding deposition of the FGM parts was carried out at the SVW80C-3D five-axis hybrid additive and subtractive manufacturing compound machining center. The VHX-1000E ultra-depth field microscope was used to observe the morphology of the mixture samples of various powders.

2.2 Experimental design

To investigate the mixing mechanism of heterogeneous powders with different morphologies in the pneumatic powder mixer, 316L gas-atomized austenitic stainless-steel powder and NiCrCoAlY Ni-based self-fluxing alloy powder with a size of 75–100 μm were selected as the key materials for powder mixing and FGM forming experiments. The 316L powder is spherical, and the NiCrCoAlY powder is irregularly rod-shaped, as shown in Fig. 4. To investigate the effect of the powder proportion on the powder mixing homogeneity, the initial feeding proportions (volumetric proportion) of 316L-NiCrCoAlY in the negative pressure powder feeder were set as the proportion of NiCrCoAlY in the mixture decreases with a gradient of 10%, and the mixture samples were obtained from the nozzles of the laser cladding head. The powder

feeding parameters are shown in Table 1. The 24 × 24 mm slides coated with epoxy resin (AB) glue were used to collect the mixed powders from the powder outlet, and six samples were taken from each group of powder mixes experiment, as shown in Fig. 5. According to the powder feeding process (Table 1), the experiment was mixed powder sampling under nine groups of proportions, as shown in Fig. 6.

In order to improve the mixing homogeneity of the pneumatic powder mixer and obtain the best mixing parameters, the influence of compression inlet angle and the number and speed on the mixing homogeneity were investigated by CFD-DEM simulation. The amount of the two powders is determined by the rotary speed (r/min) of each turntable, and the proportion of powder delivery can be controlled by adjusting the rotary speed of the turntable.

Fig. 4 Micromorphology of the 316L and NiCrCoAlY powders

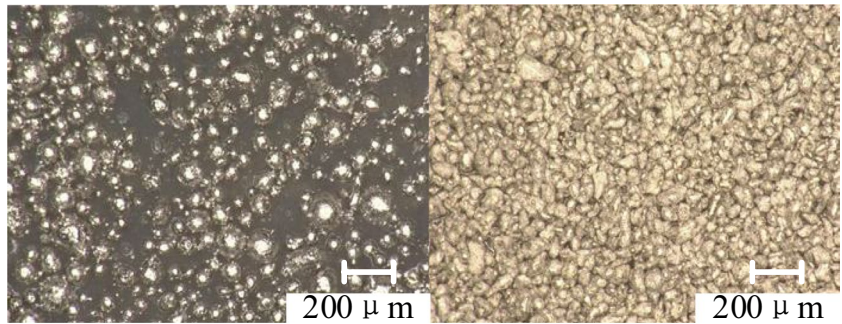


Table 1 Feeding parameters of 316L-NiCrCoAlY powders

316L (75–100 μm)			NiCrCoAlY (75–100 μm)		
Powder feeding proportion	Rotary speed (r/min)	Powder feeding rate (g/min)	Powder feeding proportion	Rotary speed (r/min)	Powder feeding rate (g/min)
10%	0.2	2.16	90%	2.11	19.40
20%	0.4	4.50	80%	1.96	18.01
30%	0.6	6.85	70%	1.74	15.99
40%	0.8	9.20	60%	1.50	13.80
50%	1.0	11.55	50%	1.25	11.55
60%	1.2	13.90	40%	1.00	9.26
70%	1.4	16.25	30%	0.75	6.96
80%	1.6	18.59	20%	0.50	4.65
90%	1.8	20.94	10%	0.25	2.33

Fig. 5 Schematic diagram of collecting mixed powder samples

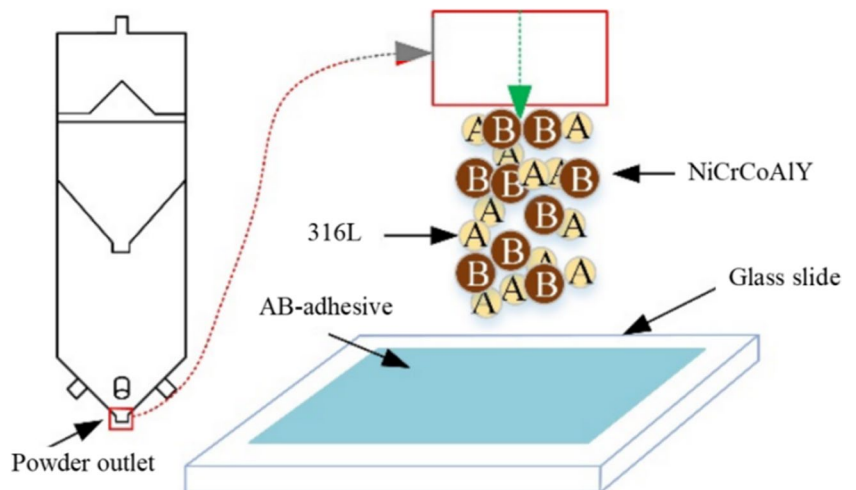
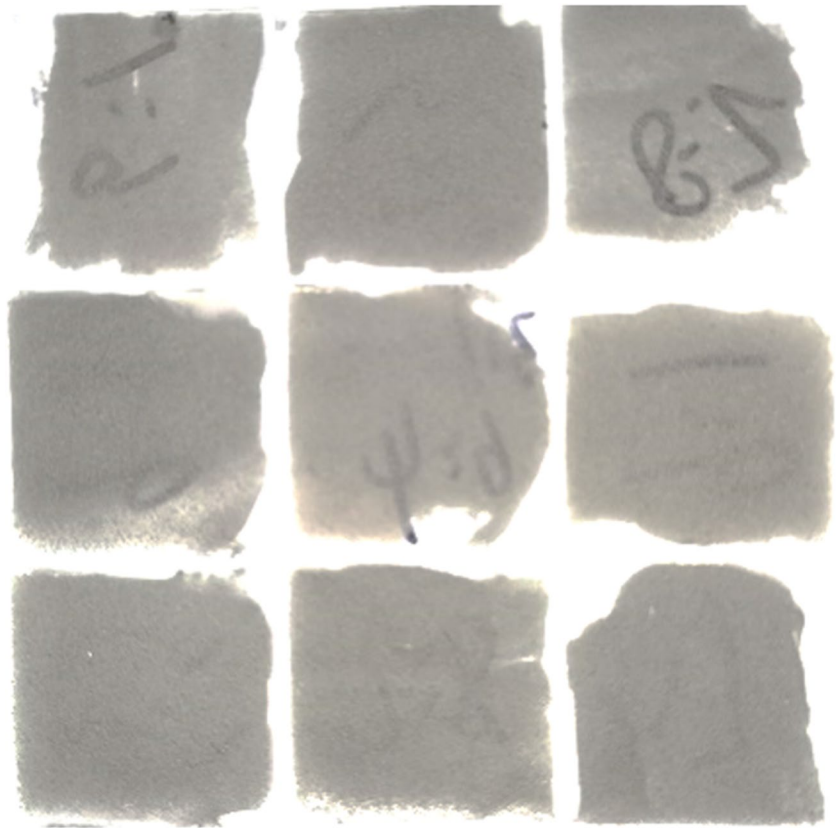


Fig. 6 Sample collected during spherical 316L (75–100 μm)-irregular NiCrCoAlY (75–100 μm)



3 CFD-DEM simulation of the powder mixing process

3.1 Assumptions

During pre-processing, the numerical simulation model of powder mixing in the pneumatic powder mixer is used. In order to improve calculative efficiency and accelerate the convergence of the gas–solid two-phase flow simulation, the employment of the simulation model is possible if:

1. The compressed nitrogen in the pneumatic powder mixer is incompressible.
2. The collision between the powders and walls of the mixer is assumed to be completely elastic.
3. The same type of powder particles have the same diameter, shape, and volume.
4. Gravity, drag force, Basset force, and pressure gradient force are considered in the force analysis of powder particles. Gravity and drag force have a significant impact on numerical analysis and determine the momentum exchange between particles and airflow. In addition, an obvious pressure gradient exists in the pneumatic powder mixer, thus the pressure gradient force acting on spherical particles should also be introduced to the simulation model.
5. The influence of buoyancy, Magnus force, and particles' self-rotation on the trajectory and collision of powder

motion can be disregarded. The ratio of buoyancy and gravity of powder in the same environment is related to the density of the powder, as per the formulas for buoyancy and gravity of powder. In the case of sparse flow, where the density ratio of 316L powder to air is greater than 1×10^3 , gravity can be disregarded. The Magnus force generated by particles' self-rotation can also be disregarded.

6. The thermal exchange between powder particles and the pneumatic powder mixer can be disregarded.

3.1.1 CFD-DEM modeling of gas–solid two-phase flow

In order to analyze the motion parameters including velocity, trajectory, and density of particles in the gas–solid two-phase flow, a CFD-DEM coupling model was established and simulated on the HP Z8 G4 workstation (CPU, Intel Xeon-5122 2.6 GHz; GPU, NVIDIA Quadro-P4000 8 GB; RAM, 64 GB DDR4). As for the continuous phase of the two-phase flow, the pneumatic powder mixer is smooth, cylindrical, and equipped with several splitter plates. The two-phase flow in the mixer is dominated by the turbulence at a relatively high Reynolds number ($Re > 2300$). In this research, the Reynolds time-averaged method was applied to the numerical simulation of turbulence with the cooperation of time-averaged flow and instantaneous pulsate flow.

The Reynolds time-averaged *N-S* governing equations [21] are listed as follows:

$$\begin{cases} \frac{\partial}{\partial x_i}(\rho u_i) = 0 \\ \frac{\partial}{\partial x_i}(\rho u_i u_j) = -\frac{\partial \rho}{\partial x_i} + \frac{\partial}{\partial x_i} \left(\mu \frac{\partial u_i}{\partial x_i} - \overline{\rho u_i' u_j'} \right) + S_i \end{cases} \quad (1)$$

where u_i and u_j are the components in the velocity direction of i and j in rectangular coordinates, μ is the dynamic viscosity of carrier gas, u_i' and u_j' are the fluctuation velocities of

turbulence, ρ is the density of carrier gas, and S_i is a custom source term.

The normal κ - ϵ equations are commonly employed in computational procedures of the two-phase flow field due to their high precision and fast convergence speed, enabling efficient solving of the turbulence model. The equations defining turbulence energy κ and dissipation rate ϵ are as follows [22]:

$$\begin{cases} \frac{\partial \rho \kappa}{\partial t} + \frac{\partial(\rho \kappa u_i)}{\partial x_i} = \frac{\partial}{\partial x_j} \left[\left(\mu + \frac{\mu_t}{\sigma_\kappa} \right) \frac{\partial \kappa}{\partial x_j} \right] + G_\kappa + G_b - \rho \epsilon - Y_M + S_\kappa \\ \mu_t = \rho C_\mu \kappa^2 / \epsilon \end{cases} \quad (2)$$

$$\frac{\partial(\rho \epsilon)}{\partial t} + \frac{\partial(\rho \epsilon u_i)}{\partial x_j} = \frac{\partial}{\partial x_j} \left[\left(\mu + \frac{\mu_t}{\sigma_\epsilon} \right) \frac{\partial \epsilon}{\partial x_j} \right] + G_{1\epsilon} \frac{\epsilon}{\kappa} + (G_\kappa + C_{3\epsilon} G_b) - C_{2\epsilon} \rho \frac{\epsilon^2}{\kappa} + S_\epsilon \quad (3)$$

where G_κ is the turbulent kinetic energy caused by the average velocity; G_b is the turbulent kinetic energy caused by buoyancy; Y_M is the coefficient of fluctuating expansion in turbulence; σ_κ is the turbulent Prandtl coefficient with the empirical value of 1.0; σ_ϵ is the coefficient corresponding to the turbulent dissipation rate, which is taken as the empirical value of 1.3; S_κ and S_ϵ are custom source terms; $G_{1\epsilon}$, $C_{2\epsilon}$, $C_{3\epsilon}$ are the empirical constants with the values of 1.44, 1.9, and 0.99, respectively; μ_t is the coefficient of turbulent viscosity; and C_μ is the coefficient related to the average strain rate, which is taken as the empirical value of 0.09 [19]. For the discrete phase model, the volume fraction in particles is usually less than 10% in the powder flow driven by carrier gas, the particles are regarded as discrete phase and the discrete phase model is adopted. The carrier gas is regarded as a continuous phase and solved by the Euler–Lagrange method. Discrete phase particle momentum equation:

$$\begin{cases} \frac{du_p}{dt} = F_D(u - u_p) + \frac{g_x(\rho_p - \rho)}{\rho_p} + F_x \\ F_D = \frac{3\mu}{\rho_p d_p^2} \frac{C_D Re_p}{4} \end{cases} \quad (4)$$

where $F_D(u - u_p)$ is the drag force and F_x is the other force acting on the solid particles. Since the particles enter the powder mixer at a constant speed with the carrier gas, the speed changes drastically after flowing through the spoiler, so the Basset force is considered; u_p is the particle velocity; ρ_p is the particle density, d_p is the average particle diameter, the relative Reynolds number is Re_p , and the drag coefficient is C_D as follows

$$Re_p = \rho d_p |u_p - u| / \mu \quad (5)$$

$$C_D = a_1 + \frac{a_2}{Re} + \frac{a_3}{Re} \quad (6)$$

where a_1 , a_2 , and a_3 are the constants set by Moris and Alexander.

The DEM model contains the collision information between particle–particle and particle–wall. Newton’s transport equation is calculated to describe particle movement,

$$m \frac{du_p}{dt} = \sum F_i = F_g + F_{con}^n + F_{con}^t + F_{adh} \quad (7)$$

$$I_p \frac{dw_p}{dt} = T_p + r_p F_{con}^t \quad (8)$$

where F_g is the force of gravity on particles; F_{con}^n is the normal contact force between particles; F_{con}^t is the tangential contact force between particles; F_{adh} is the adhesion between fluids; and I_p , T_p , and w_p are the inertia, torque, and angular velocity of a particle, respectively.

3.1.2 Kinematic analysis of gas–solid two-phase flow by CFD simulation

3.1.2.1 Influence of compression inlet angle In this experiment, the two-phase flow under various compression intake angles was analyzed by using CFD simulation, resulting in the visualization of velocity cloud and particle trace of compressed air. The cone at the base of the mixer was squeezed in three directions: 90°, 45°, and 0°, with a compression input velocity of 1 m/s. Additionally, 2, 4, and 8 compression inlets were utilized.

Figure 7 shows that the velocity direction of the compressed air inlet is parallel to the velocity direction of the two-phase flow as it passes through the conflux plate when the air inlet is compressed at a vertical angle of 90°. There is no horizontal velocity component to the compressed air inlet. Based on the color distribution in Fig. 7d, it is evident that the velocity at the exit is not uniform and that the compressed intake has minimal effect on the two-phase

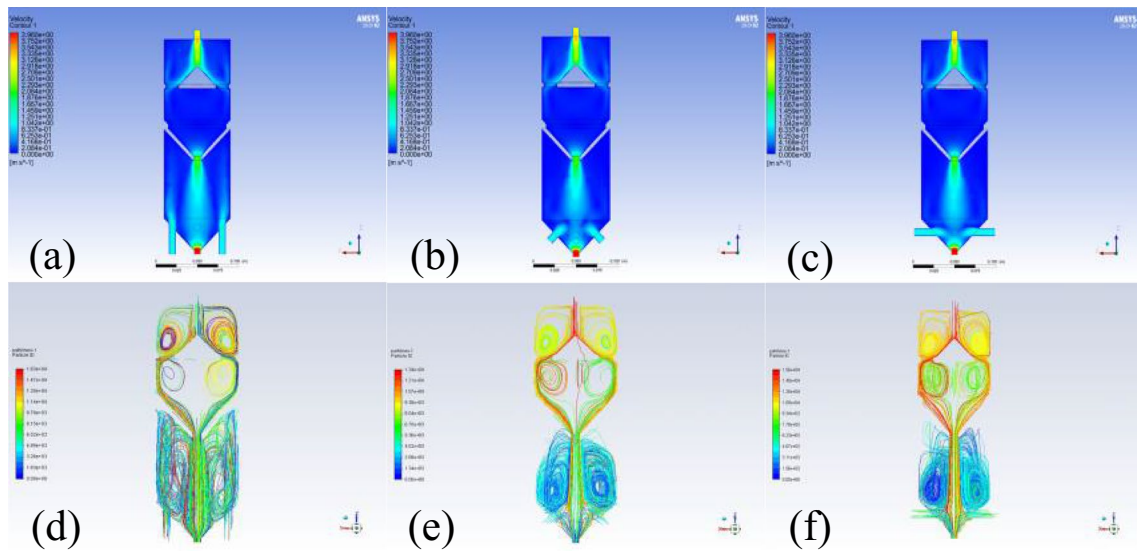


Fig. 7 Velocity cloud and particle trace of two-phase flow with various inlet orientations: **a** and **d** vertical 90°, **b** and **e** tilt 45°, and **c** and **f** horizontal 0°

flow, making it unfavorable for further powder mixing. The velocity direction of the compressed air inlet is horizontal when it is at 0°, and the compressed air in the inlet directly prevents symmetrical compression of the air inlet. Although the collision motion of the particle swarm is conducive to breaking the interaction between particles and enhancing particle mixing [1], compressed air does not carry particles. Conversely, the pure compressed gas increases convection and squeezes the mixed two-phase flow. Thus, the inlet orientation at 0° should be avoided. When the air inlet is slanted at 45°, the velocity of the air inlet has horizontal and vertical components. The horizontal component creates

a disturbance to the two-phase flow, causing some particles to diffuse, while the vertical component raises the position of the convergence point of the compressed air and the mixed two-phase flow from the confluent plate. The diffusion movement of particles promotes fine mixing, improves local mixing quality, and helps to further enhance powder mixing.

3.1.2.2 Influence of compression inlet number According to Fig. 8, an increase in the number of compression inlets leads to a corresponding increase in fluid velocity at the outlet. Additionally, it can be observed that while keeping the volume constant, an increase in the molar amount of gas fill-

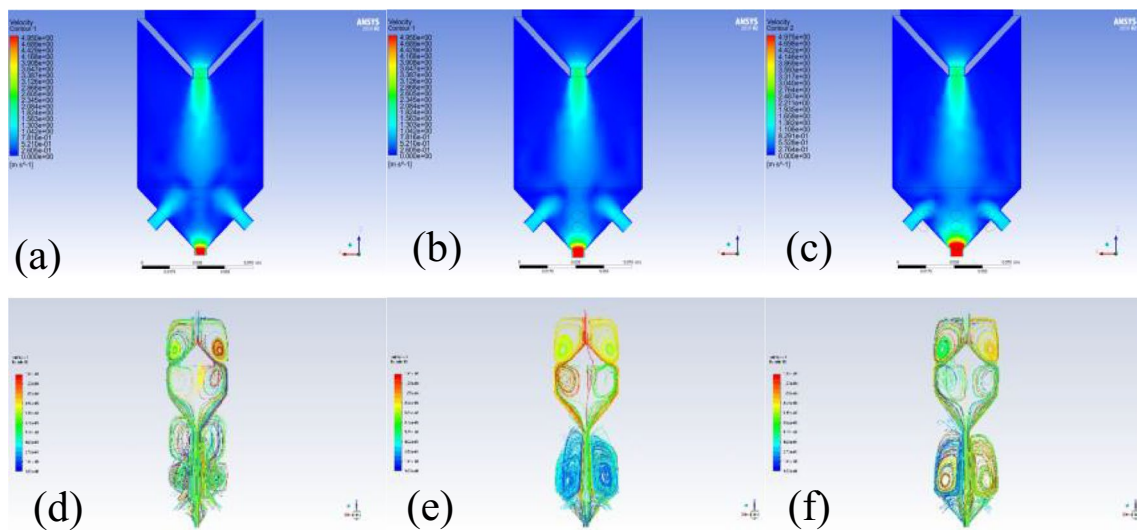


Fig. 8 Velocity contours and particle traces with 2 (**a** and **d**), 4 (**b** and **e**), and 8 (**c** and **f**) compression inlets

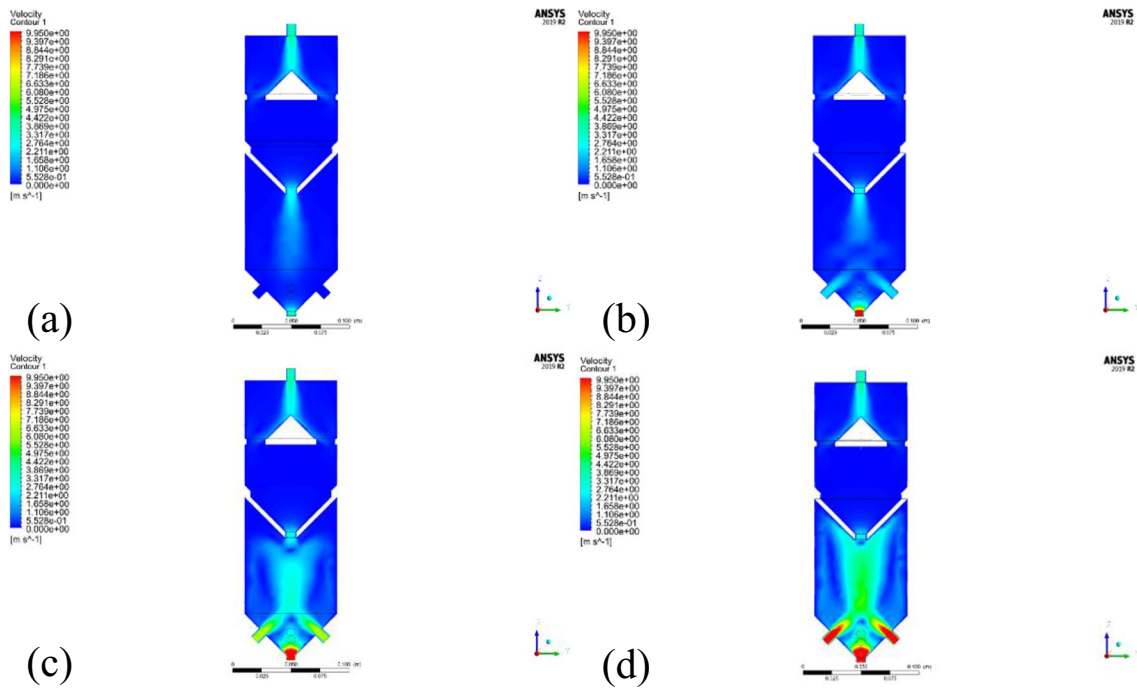


Fig. 9 Velocity contours at different compressed inlet velocities a 0 m/s, b 3.0 m/s, c 6.0 m/s, and d 10.0 m/s

ing the container increases the pressure inside the container. The velocity of the two-phase flow at the outlet is determined by both the gas pressure and the viscous resistance generated from the friction between the mixer’s wall and gas. Thus, increasing the number of compression inlets can enhance fluid velocity at the outlet. According to Fig. 8a and d, when there are two compression inlets, the low fluid velocity leads to inadequate mixing in the area between the conflux plate and compression inlets. When using 4 and 8 compression inlets, the fluid velocity and accelerated velocity of the two-phase flow are significantly increased, thereby increasing the shear effect, which is conducive to powder mixing.

3.1.2.3 Influence of compression inlet velocity To investigate the impact of compression inlet velocity on the powder mixing quality, a larger gas flow rate within a reasonable range can accelerate the mixing process, according to the experimental results from Wang et al. [20]. Therefore, different flow velocity settings of 0, 3.0, 6.0, and 10.0 m/s were adopted for compressed air intake. As shown in Fig. 9a and b, as the compression inlet velocity increases, the driving force of the two-phase flow exiting the conflux plate also increases, thereby promoting a greater displacement of the two-phase flow. This increased displacement expands the mixing range and improves convective mixing efficiency. However, when the compression inlet velocity exceeds 3 m/s

Table 2 EDEM numerical simulation parameters

Parameter	316L	NiCrCoAlY
Density (g/cm ³)	7.8	7.3
Radius of spheres (μm)	75	75
Shear modulus (Pa)	1 × 10 ⁸	1 × 10 ⁸
Poisson ratio	0.25	0.25
Static friction	0.5	0.5
Initial velocity(m/s)	2	2
Time step (s)	5 × 10 ⁻⁷	5 × 10 ⁻⁷

(Fig. 9c and d), it exceeds the initial velocity of the two-phase flow, and the reverse compression inlet delays the outflow of the two-phase flow through the conflux plate. Excessive compressed air intake exceeding initial velocities also generates significant uncontrolled disturbances. In this context, the drag force increases and impedes adequate powder mixing.

3.1.3 Kinematic analysis of gas–solid two-phase flow by CFD-DEM coupling simulation

By analyzing the influence of inlet speed, angle, and quantity on the pneumatic powder mixer with CFD simulation, we were able to determine the optimal configuration of the pneumatic powder mixer. The installation distance of adjacent spoiler

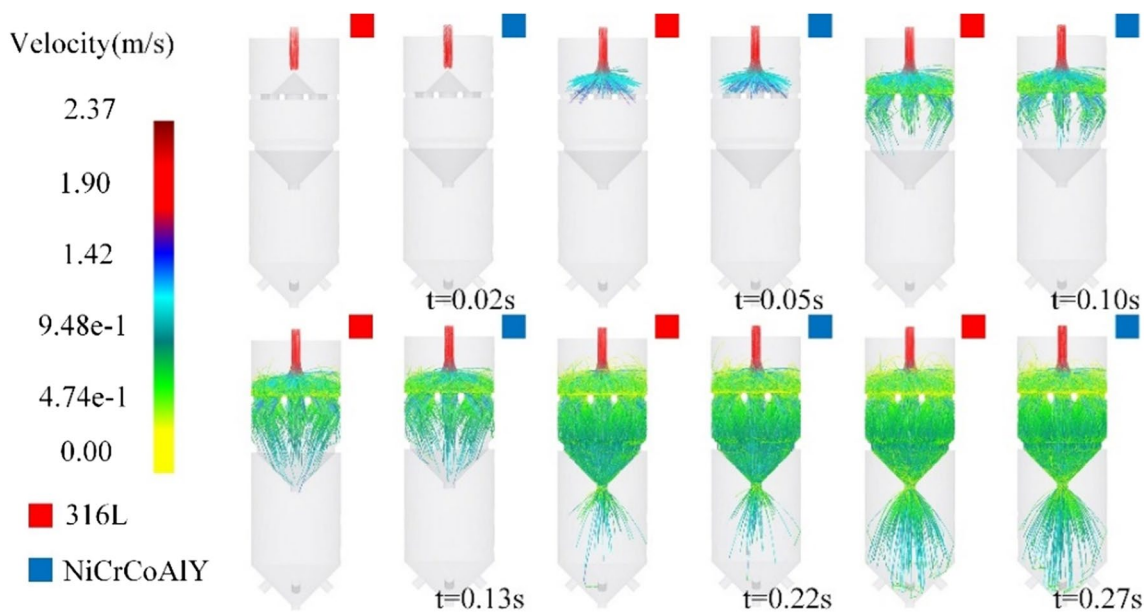


Fig. 10 Particle trace diagrams of 316L and NiCrCoAlY in 0–0.27 s

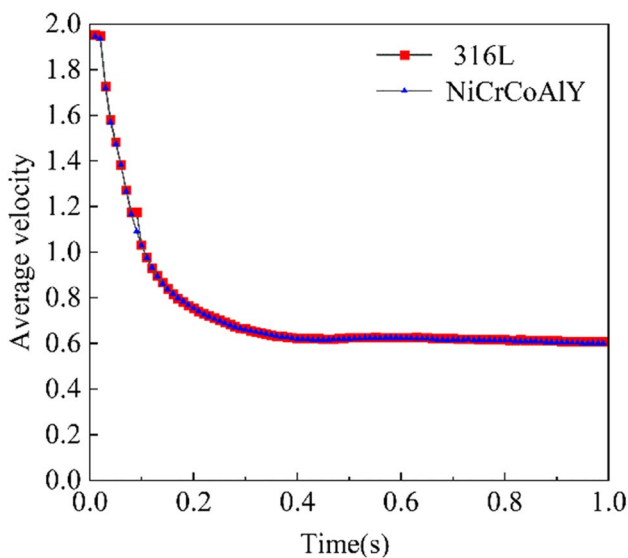


Fig. 11 Average velocity of 316L and NiCrCoAlY powders in 0–1 s

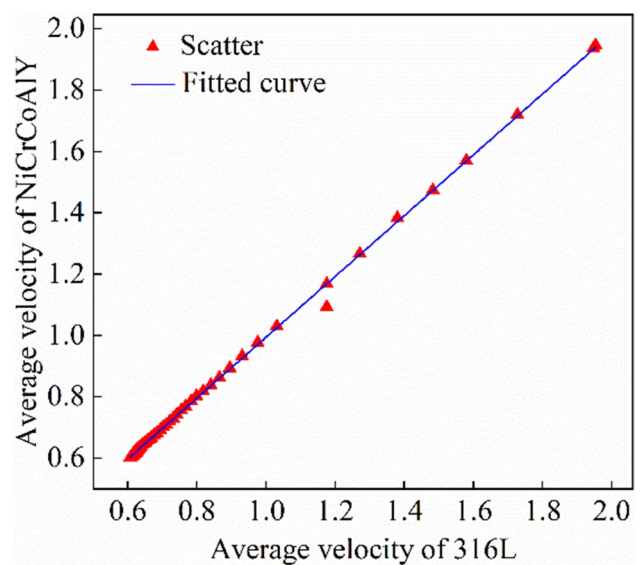


Fig. 12 Relationship of average velocity between 316L and NiCrCoAlY at the same time

plates is 45–50 mm. Four compressed air inlets with an entry angle of 45° are utilized. In this section, kinematic analysis of gas–solid two-phase flow including average velocity, particle number at the outlet, and axial particle number throughout the mixer was analyzed by using CFD-DEM coupling simulation. Specifically, the initial inlet velocity is set at 3 m/s while the compressed inlet velocity is maintained at 2 m/s. For solid-phase materials, we employed 316L and NiCrCoAlY alloys, whereas air was used as the gas-phase medium. The initial

gas velocity is set to 3 m/s and the particle velocity to 2 m/s, respectively, with a time step interval of 5×10^{-7} s. Parameters applied to EDEM numerical simulation are shown in Table 2.

3.1.3.1 Average velocity of two-phase flow After conducting EDEM post-processing for CFD-DEM coupling simulation, particle trace diagrams were obtained as depicted in Fig. 10. To validate the homogeneity of pow-

der mixing, a functional relationship between the average velocities of 316L and NiCrCoAlY powders in the 0–1 s time range was simulated. The scatter plot of the average velocity of 316L-NiCrCoAlY over time is shown in Fig. 11. The relationship of average velocity between 316L and NiCrCoAlY at the same time is fitted by Origin and the results are shown in Fig. 12. The equation of the fitted curve is as follows:

$$y = 0.992247x + 0.001510832 \tag{9}$$

According to Fig. 12, there is a positive correlation between the average velocity of 316L and NiCrCoAlY, demonstrating a linear relationship. The actual fitting slope of

Eq. (9) is up to 0.992, indicating that the average velocities and displacement of both materials are similar. This similar displacement increases the probability of powder contact, thereby promoting convective mixing by changing the mutual position of neighboring particles.

3.1.3.2 Particle number at outlet In addition to the spatial variation of mixing components, it is also crucial to consider the homogeneity of components at the outlet because the uniformity of particle mixing at the outlet significantly impacts additive manufacturing quality. The particle numbers of 316L and NiCrCoAlY within 0.35–1 s at the powder outlet were statistically calculated as shown in Table 3. In

Table 3 Particle number and mean value of the 316L fragment within 0.35–0.99 s

Times (s)	316L particle number	NiCrCoAlY particle number	Sum of particle number	Proportion of 316L	Times (s)	316L particle number	NiCrCoAlY particle number	Sum of particle number	Proportion of 316L
0.35	11	8	19	0.5789	0.68	336	320	656	0.5122
0.36	11	9	20	0.5500	0.69	352	318	670	0.5254
0.37	16	9	25	0.6400	0.7	357	308	665	0.5368
0.38	18	15	33	0.5455	0.71	320	321	641	0.4992
0.39	21	15	36	0.5833	0.72	318	341	659	0.4825
0.4	24	21	45	0.5333	0.73	338	363	701	0.4822
0.41	24	21	45	0.5333	0.74	373	322	695	0.5367
0.42	35	28	63	0.5556	0.75	341	325	666	0.5120
0.43	42	36	78	0.5385	0.76	319	319	638	0.5000
0.44	50	52	102	0.4902	0.77	338	331	669	0.5052
0.45	66	50	116	0.5690	0.78	365	335	700	0.5214
0.46	64	58	122	0.5246	0.79	348	354	702	0.4957
0.47	76	115	191	0.3979	0.8	342	318	660	0.5182
0.48	101	89	190	0.5316	0.81	327	350	677	0.4830
0.49	150	114	264	0.5682	0.82	315	314	629	0.5008
0.5	153	126	279	0.5484	0.83	369	338	707	0.5219
0.51	148	166	314	0.4713	0.84	319	326	645	0.4946
0.52	207	177	384	0.5391	0.85	350	318	668	0.5240
0.53	221	238	459	0.4815	0.86	351	356	707	0.4965
0.54	250	219	469	0.5330	0.87	344	342	686	0.5015
0.55	289	239	528	0.5473	0.88	371	355	726	0.5110
0.56	286	260	546	0.5238	0.89	343	351	694	0.4942
0.57	320	290	610	0.5246	0.9	336	342	678	0.4956
0.58	306	283	589	0.5195	0.91	326	345	671	0.4858
0.59	323	331	654	0.4939	0.92	350	342	692	0.5058
0.6	348	315	663	0.5249	0.93	350	326	676	0.5178
0.61	320	323	643	0.4977	0.94	350	357	707	0.4950
0.62	358	359	717	0.4993	0.95	335	316	651	0.5146
0.63	351	343	694	0.5058	0.96	364	336	700	0.5200
0.64	379	350	729	0.5199	0.97	335	365	700	0.4786
0.65	353	340	693	0.5094	0.98	344	323	667	0.5157
0.66	319	351	670	0.4761	0.99	352	363	715	0.4923
0.67	353	343	696	0.5072	1	350	372	722	0.4848

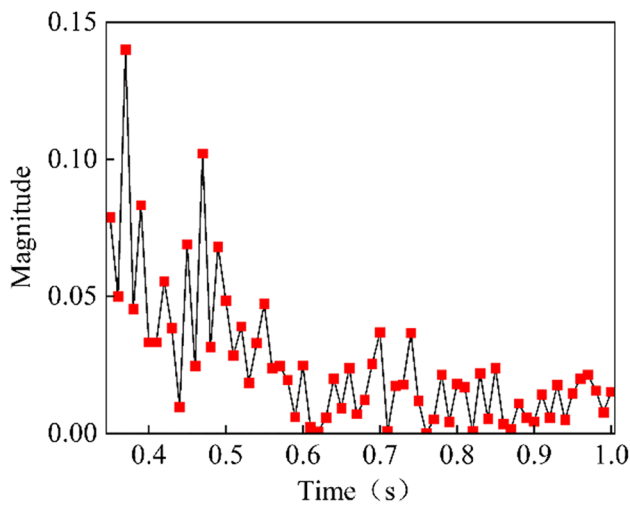


Fig. 13 Electric wire diagram of deviation absolute value of 316L particle proportion at the outlet

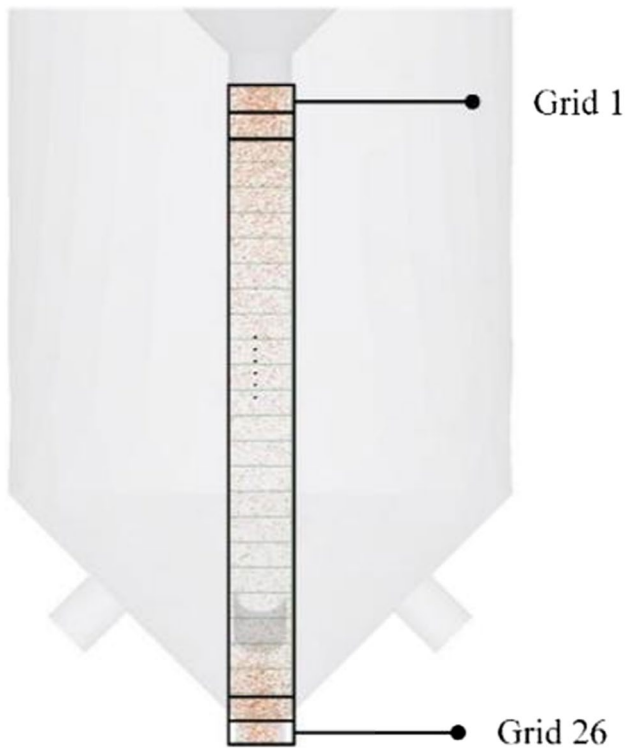


Fig. 14 Schematic diagram of axial equipartition

In addition to the spatial variation of mixing components, it is also crucial to consider the homogeneity of components at the outlet because the uniformity of particle mixing at the outlet significantly impacts additive manufacturing quality.

The statistical calculation in Table 3 presents the particle counts of 316L and NiCrCoAlY within the range of 0.35–1 s at the powder outlet. Due to the use of equal volume mixing, in Table 3, the ratio of 0.5 is the ideal value, indicating that the two powders are completely evenly mixed. The mean square error is calculated for the data in Table 5, indicating the degree of deviation of 316L particles from the ideal value, so as to compare the uniformity of powder mixing.

$$MSE = \sum (e_i)^2 / n \tag{10}$$

where e_i is the deviation value of 316L particle number proportion corresponding to different moments at the powder outlet and n is the number of 316L particles.

Since 0.05 is only 10% of 0.5, 0.05 is taken as the cutoff point, and the part below 0.05 can be regarded as within the error range. According to Fig. 13, the absolute deviation value of the proportion of 316L particles at the outlet shows a decreasing trend with time, which means that the outlet can continuously output a two-phase flow with the mixing quality within a low error range after a certain period of time.

3.1.3.3 Axial particle number throughout the mixer The particle counting was conducted at the axial distance from the exit of the poly-flow plate to the powder outlet. The Grid Bin Group was divided into 26 equal parts in the z -direction along this axial distance, and the schematic diagram illustrating these equal parts is shown in Fig. 14 below. The particle numbers of 316L and NiCrCoAlY within the axial distance range of 0–1 s were obtained. Some sections of the grid did not have particles passing through during the pre-simulation period, and data information within 0.35–1 s was retained for analysis purposes. Because the two-phase flow moves from the top down, in the beginning for, a short period of time, there are no particles at the portion of the grid at the bottom of the mixer. Through experiments and observations, counting from 0.35 can ensure that all the grids have particles, resulting in the determination of the proportion of 316L particles in each of the 26 groups within the grid at different time points, as depicted in Figs. 15 and 16 below.

According to Figs. 15 and 16, it can be observed that there is an initial increase followed by a subsequent decrease trend in mean square error with increasing grid number. It is available in Table 4, $MSE_{26} = 1.16 \times 10^{-3}$ for the proportion of 316L particles under grid number 20 is already smaller than $MSE_1 = 1.371 \times 10^{-3}$ for the proportion of 316L particles under grid number 1. This indicates that at distances ranging from the outlet of the converging plate to the powder outlet, mixing homogeneity initially decreases before showing an improvement trend.

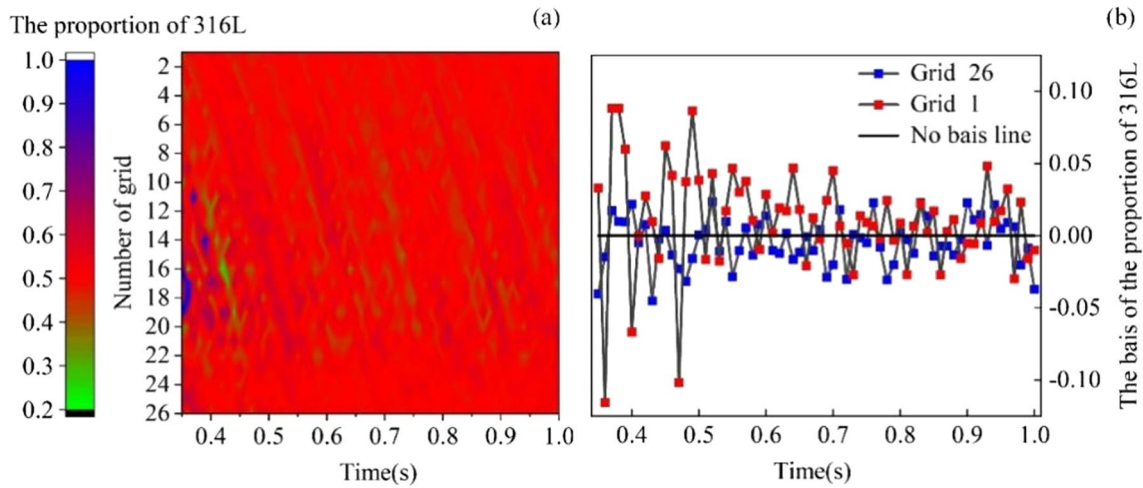


Fig. 15 **a** The contour diagrams of the proportion of 316L particles at the powder outlet within 0.35–1 s and **b** the deviation value point line map of the proportion of 316L particles in Grid 26 and Grid 1 within 0.35–1 s

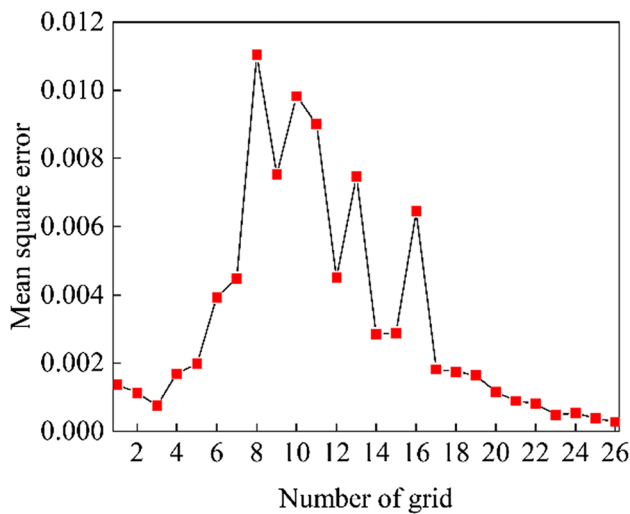


Fig. 16 Mean square deviation of 316L particle proportion under different Grid numbers

Within the 0.35–1 s time frame, $MSE_{26} = 2.87 \times 10^{-4}$ for the proportion of 316L particles under grid number 26 is smaller than $MSE_1 = 1.371 \times 10^{-3}$ for the proportion of

316L particles under grid number 1, suggesting that the proportion under grid number 26 is closer to the ideal value (0.5). In other words, compressed input air contributes to enhancing mixing homogeneity to some extent. Powder mixing homogeneity at the outlet surpasses that at the collector plate. The two-phase flow through the collector plate improves the mixing homogeneity under the gas perturbation of the compressed inlet gas, thus validating the feasibility of using the gas perturbation technique for improving the quality of the gas–solid two-phase flow mixture.

4 Experiment and discussion

4.1 Evaluation of mixing quality

The parameter used to evaluate the quality of mixing is mixing uniformity. In mathematics, the commonly used method to evaluate the quality of powder mixing is the mathematical statistics method. The dispersion (coefficient of variation) of the sample data is used to describe the uniformity of the mixed powder. The smaller the dispersion value, the

Table 4 Mean square error of 316L—the proportion of the number of particles of 316L for Grids 1–26

Grid number	Mean square error	Grid number	Mean square error	Grid number	Mean square error	Grid number	Mean square error
1	0.001371	8	0.011043	15	0.002879	22	0.00082
2	0.001133	9	0.00753	16	0.00646	23	0.00048
3	0.00076	10	0.009834	17	0.00183	24	0.00054
4	0.001697	11	0.009012	18	0.001753	25	0.00038
5	0.001998	12	0.004512	19	0.001647	26	0.00029
6	0.00394	13	0.007477	20	0.00116		
7	0.004497	14	0.002861	21	0.000898		

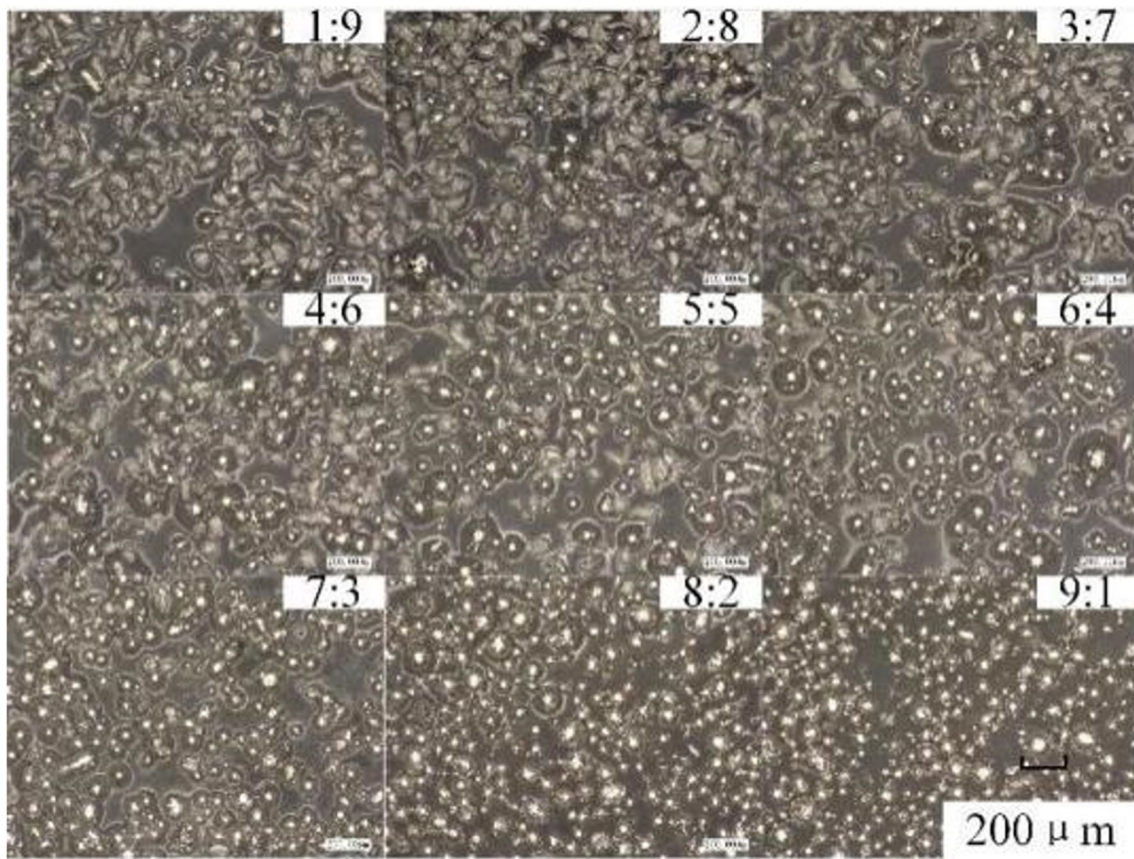


Fig. 17 Microstructure of 316/NiCrCoAlY mixed powder samples with different proportions

Table 5 Mean value, standard deviation and coefficient of variation of 316L particle number percentage

Proportion of 316L	Mean value	Standard deviation	Coefficient of variation
0.1	0.11875	0.003403	2.87%
0.2	0.19175	0.037995	19.81%
0.3	0.316	0.007874	2.49%
0.4	0.40825	0.014221	3.48%
0.5	0.5	0	0.00%
0.6	0.617	0.027928	4.53%
0.7	0.75925	0.05704	7.51%
0.8	0.78375	0.002062	0.26%
0.9	0.89425	0.01201	1.34%

higher the uniformity of the mixed powder. A total of n samples are taken from the experimentally obtained powder to create a complete sample, and the content of a specific component in each sample is denoted as X_i . The mean \bar{X} and standard deviation S of the content of the specific component in the sample are:

$$\bar{X} = \frac{1}{n} \sum_{i=1}^n X_i \tag{11}$$

$$S = \sqrt{\frac{1}{n-1} \sum_{i=1}^n (X_i - \bar{X})^2} \tag{12}$$

In the formula, n is the number of powder specimens extracted in the experiment and X_i is the content of a certain component in each sample.

The mean value of the sample X_i represents the average content of a certain component in the mixture; the standard deviation S represents the fluctuation range of a certain component's content. According to the mean \bar{X} and standard deviation S of the sample, the dispersion R can be obtained as follows:

$$R = (S/\bar{X}) \times 100\% \tag{13}$$

4.2 Powder mixing experiment

According to Table 1 in Sect. 2, 316L and NiCrCoAlY powders were input in different proportions to carry out nine

Fig. 18 Histogram of variation coefficient of 316L particle count ratio

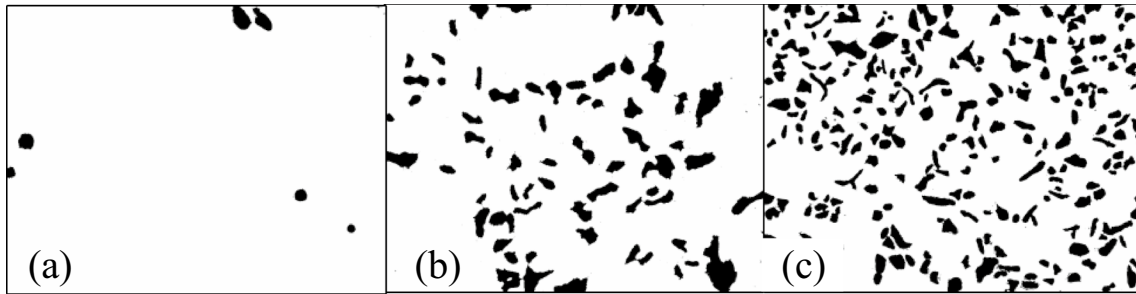
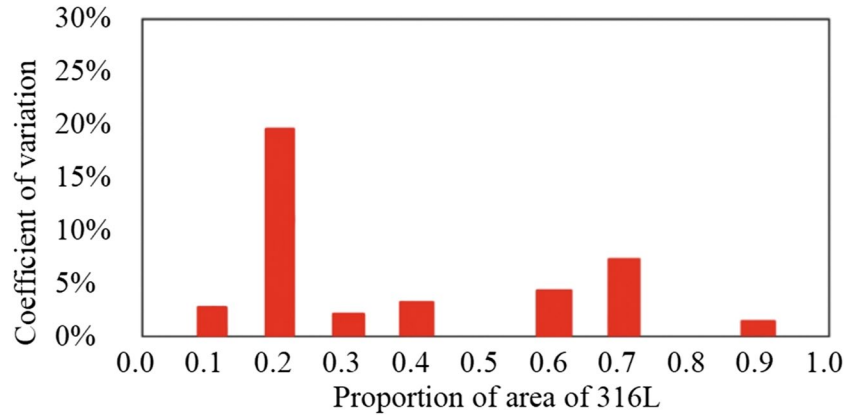


Fig. 19 ImageJ processing graph under area counting: **a** NiCrCoAlY mapping with 316L ratio of 0.1, **b** NiCrCoAlY mapping with 316L fraction of 0.5, and **c** NiCrCoAlY mapping with 316L ratio of 0.9

Table 6 Mean value, standard deviation, and coefficient of variation of 316L area ratio

Proportion of 316L	Mean value	Standard deviation	Coefficient of variation
0.1	0.0195	4.655×10^{-3}	23.87%
0.2	0.02025	10.308×10^{-3}	50.90%
0.3	0.01525	5.56×10^{-3}	36.46%
0.4	0.241	28.272×10^{-3}	11.73%
0.5	0.50375	13.226×10^{-3}	2.63%
0.6	0.6105	21.672×10^{-3}	3.55%
0.7	0.693	25.871×10^{-3}	3.73%
0.8	0.83125	15.756×10^{-3}	1.90%
0.9	0.85675	16.256×10^{-3}	1.90%

sets of experiments. The 24×24 mm slide after AB glue was applied was used for powder mixing collection, and six samples were collected in each group. The microscopic morphology collected by super depth of field is shown in Fig. 17.

The microscopic morphology images taken with the super depth of field image of powder mixing sampling are

processed by image to obtain the proportion of 316L and NiCrCoAlY particles. One optimal value and one worst value of the six samples' data in each group of powder mixing experiments are removed. The remaining data are statistically shown in Table 5 and Fig. 18.

The super depth of field map of powder mixing sampling is processed by ImageJ as shown in Fig. 19, and the area ratio of 316L and NiCrCoAlY is obtained. One optimal value and one worst value of six sample data in each group of powder mixing experiment are removed. The remaining data are statistically as follows in Table 6.

In order to further verify the accuracy of the experimental results of the particle size difference mixing powder, the 316L-NiCrCoAlY mixing powder samples with 316L content of 0.1, 0.5, 0.7, 0.8, and 0.9 were subjected to EDS. The elemental distribution of Fe was marked in green, and the elemental distribution of Ni was marked in red as shown in Fig. 20. The particle counting information and analytical data were shown in Table 7.

Tables 5 and 7 utilize the particle number proportion to analyze the homogeneity of powder mixing. The difference between the data of 316L particle number ratio in the two tables is small, which can prove that it is feasible

Fig. 20 EDS results of 316L-NiCrCoAlY mixture with 316L content of 0.1, 0.5, 0.7, 0.8, and 0.9 (a, d, g, j, and m) EDS layered images; Fe elements (b, e, h, k, and n); and Ni elements (c, f, i, l, and o)

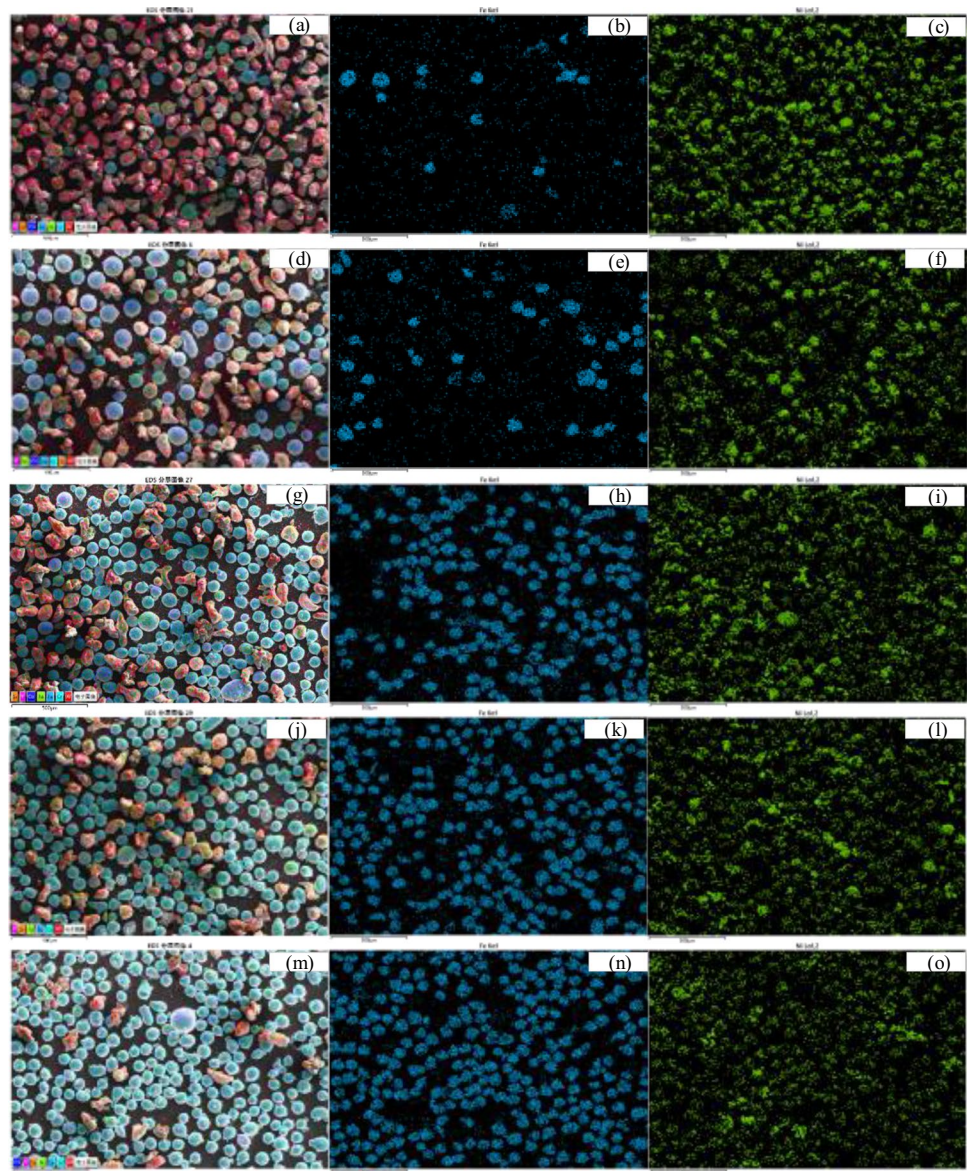


Table 7 Mean value, standard deviation, and coefficient of variation of 316L area ratio

Proportion of 316L	316L particle number	NiCrCoAlY particle number	Proportion of 316L particle number
0.1	25	171	0.128
0.5	66	69	0.489
0.7	198	79	0.715
0.8	230	63	0.785
0.9	267	25	0.914

to process the super depth-of-field map of powder mixture sampling with ImageJ, and the experimental results have high accuracy. According to Figs. 21 and 22, the coefficient

of variation obtained by the particle counting method is smaller than that obtained by the area-counting method, and histogram 18 shows that when the ratio of 316L is at its highest point (0.2), it exhibits a coefficient variation value at its largest with a percentage value equaling 19.81%. When the 316L ratio is 0.5, the coefficient of variation is the smallest, with a value of 0%. When the ratios of 316L ranged from 0.1 to 0.9, the coefficient of variation values were all lower than 20%, 8 groups were below 10%, and 7 groups were below 5%. Based on the aforementioned data, analysis reveals: (1) The coefficient of variation value decreases as the proportion of 316L increases for different mixing ratios and data processing methods, indicating an improved mixing effect for 316L-NiCrCoAlY. (2) When using ImageJ to process microscopic images, the area

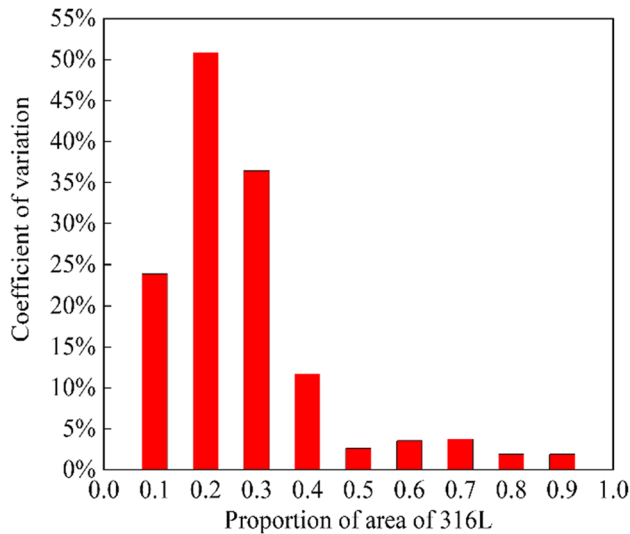


Fig. 21 Histogram of coefficient of variation of 316L area proportion

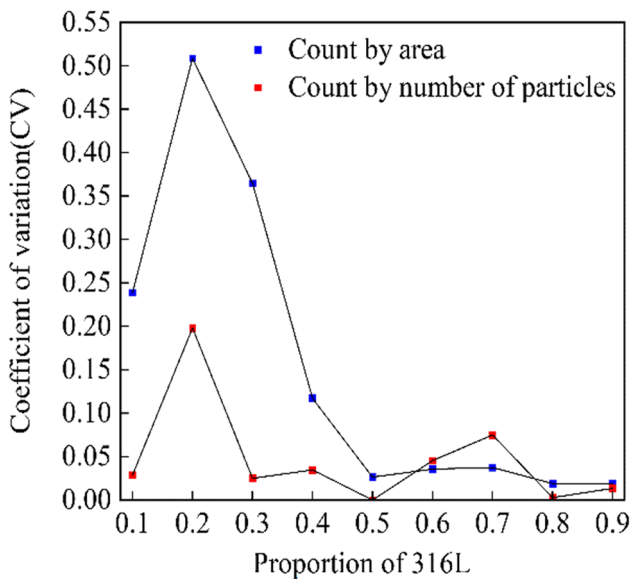


Fig. 22 Ratio of 316L by different counting methods—coefficient of variation line chart

counting method identifies areas based on image brightness, resulting in smaller areas than their actual values; thus, the obtained area for 316L is underestimated. As shown in Table 6, after data processing, there is a higher coefficient of variation for the ratio of 316L area compared to the particle counting method. Therefore, this counting method has larger errors compared to the particle counting method and should be considered less reliable.

4.3 L-DED forming experiment

In this subsection, in order to further explore the effect of powder mixing uniformity on the micro-morphology of L-DED specimens, ten single-pass cladding layers made of spherical 316L (75–100 μm) and non-spherical NiCrCoAlY (61–75 μm , 75–100 μm) were formed under five feeding ratios (0.1, 0.3, 0.5, 0.7, 0.9), and the experimental conditions are shown in Table 8. The micro-morphology of the cladding single-pass section with the particle size difference between the powder mixing group and the comparison group was obtained by ultra-depth of field.

According to subsection 3.4.2, the mixing uniformity of spherical 316L (75–100 μm) and non-spherical NiCrCoAlY (75–100 μm) powder with a 316L content of 0.5 is the best. The comparison between Fig. 23c and f shows obvious grain boundaries at the bottom of the cladding single channel in the group with different particle sizes. Analysis reveals that NiCrCoAlY with different particle sizes has varying ejections through the cladding head and different heat absorption per unit mass. Heat near both sides of the cladding single channel has a greater chance of dissipating through air convection, apart from being lost through the substrate. Due to multi-directional heat transfer, the component of the temperature gradient along the deposition height is no longer dominant, resulting in anisotropic dendrites forming clear grain boundaries where cracks are likely to appear and expand, reducing strength in this area. In contrast, in groups without particle size differences, full and robust short dendrites first grow on the coating bottom. Some of these short dendrites extend into longer ones along the deposition direction. Combined with Fig. 23b and e, groups without particle size differences exhibit a denser grain arrangement, uniform and complete short dendrite sizes, as well as better hardness and strength. Through the analysis of the top section of cladding single channels using Fig. 23a and d, it is observed that in groups Fig. 23a without particle size differences, long straight dendritic crystals still permeate even at the top, which significantly enhances plasticity in this region.

The experimental results show that the larger grain exhibits stronger lasting strength and creep strength and a smaller creep rate, while the smaller grain has higher tensile strength and fatigue strength. The non-spherical powder has poor fluidity, lower heat absorption stability per unit mass compared to spherical powder, and less growth of dendritic crystals but more equiaxed crystals. This leads to reduced plasticity in the material.

When the proportion of 316L is 0.5, the mixing effect is the best, and when the particle size of 316L powder and NiCrCoAlY powder is the same, the strength, hardness, and plasticity of the material are optimal. Larger and fuller crystals were visible in the micromorphology with good mixing uniformity, large grains have strong

Table 8 Spherical 316L (75–100 μm)–irregular NiCrCoAlY (75–100 μm and 61–75 μm) forming process (with and without the mixer)

316L (75–100 μm)		NiCrCoAlY (75–100 μm)			NiCrCoAlY(61–75 μm)	
Powder feeding proportion	Rotary speed (r/min)	Powder feeding proportion	Rotary speed (r/min)	Rotary speed (r/min; without mixer)	Rotary speed (r/min)	Rotary speed (r/min; without mixer)
0.1	0.5	0.9	2.25	4.03	3.20	3.22
0.2	1.0	0.8	1.90	3.65	2.53	2.93
0.3	1.5	0.7	1.62	2.82	2.01	2.30
0.4	2.0	0.6	1.35	2.22	1.67	1.84
0.5	2.5	0.5	1.08	1.71	1.40	1.44
0.6	3.0	0.4	0.83	1.24	1.16	1.09
0.7	3.5	0.3	0.57	0.80	0.95	0.75
0.8	4.0	0.2	0.31	0.38	0.75	0.43
0.9	4.5	0.1	0.06	0.10	0.56	0.11

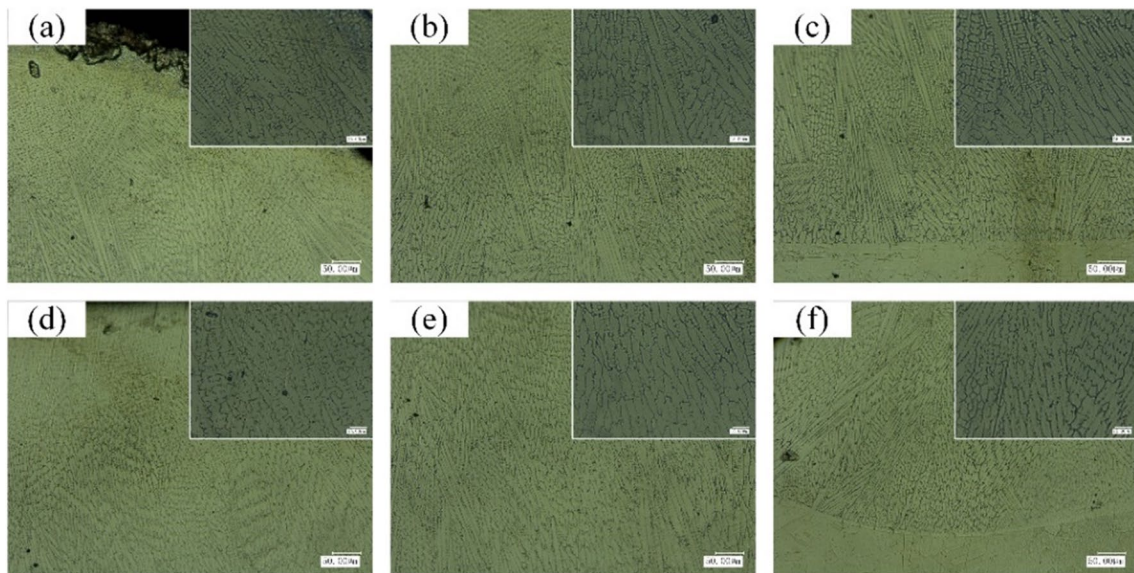


Fig. 23 Comparison of the top, middle, and bottom of the cladding single channel of spherical 316L (75–100 μm)–non-spherical NiCrCoAlY (75–100 μm) and spherical 316L (75–100 μm)–non-spherical NiCrCoAlY (61–75 μm) with density difference

persistent strength and creep strength, and the crystals in the microtissue are denser and have better hardness. Therefore, improving the mixing uniformity of the powder has a good effect on improving the lasting strength and hardness.

5 Conclusion

In this paper, the pneumatic mixing of 316L–NiCrCoAlY is simulated, and the powder mixing and forming experiments are carried out. Improving the mixing uniformity of the powder mixer has a positive effect on enhancing the lasting strength and hardness. The study focuses on the powder mixing ratio and forming performance under the selected configuration. The following conclusions have been drawn:

1. The numerical analysis method can effectively describe the heterogeneous particle mixing rule. The designed pneumatic powder mixer can improve the mixing homogeneity of 316L and NiCrCoAlY powders. The compression inlet velocity should not exceed the initial velocity of the two-phase flow. The horizontal and vertical components generated by the 45° compression inlet are more conducive to the formation of favorable disturbances to the two-phase flow, and the number of 4 and 8 compression inlets with uniform action on the flow field is more appropriate.
2. The average velocity of 316L particles and the average velocity of NiCrCoAlY particles showed a positive linear relationship at the same time, and the slope of the fit, 0.9925, was very close to 1. The average velocity of

316L and NiCrCoAlY were close to each other, and the displacement values at the same time were also close. The close displacement values increase the opportunity for particle contact, which is beneficial for improving the mixing homogeneity.

3. The mean square error of the percentage of 316L particles at the powder outlet in the range of 0.35–1 s tends to decrease, indicating that the two-phase flow with the mixed powder quality in the low error range can be continuously output after a certain time.
4. At the axial distance from the outlet of the poly-flow plate to the powder outlet, the mixing quality gradually improves with increasing time. The mean square error $MSE_{26} = 0.000287$ to the number of 316L particles at the outlet is smaller than the mean square error $MSE_1 = 0.001371$ at the exit of the poly-flow plate, and the powder mixing quality is significantly improved after the gas disturbance of the compressed inlet air.
5. According to the data processing results obtained using the particle proportion counting method, the preset value for the mixing proportion of non-spherical particles should be increased when the proportion of spherical particles is low. This can effectively enhance the homogeneity of powder mixing.

Author contribution Bo Xin: conceptualization, methodology, supervision, writing—review and editing, and funding acquisition. Yuting Wang: investigation, data curation, writing—original draft, and validation. Wenfu Zhu: formal analysis and data curation. Jiaxin Qin: formal analysis and data curation. Gang Cao: data curation.

Funding This research was financially supported by the National Nature Science Foundation (Grant No. 52005093) and the Natural Science Foundation of Liaoning Province (Grant No. 2023-MS-085), PR China. Both projects are led by Bo Xin.

Declarations

Competing interests The authors declare no competing interests.

References

1. Ayan Y, Kahraman N (2022) Fabrication and characterization of functionally graded material (FGM) structure containing two dissimilar steels (ER70S-6 and 308LSi) by wire arc additive manufacturing (WAAM). *Mater Today Commun* 33:104457. <https://doi.org/10.1016/j.mtcomm.2022.104457>
2. Chen L, Yu T, Chen X, Zhao Y, Guan C (2022) Process optimization, microstructure and microhardness of coaxial laser cladding TiC reinforced Ni-based composite coatings. *Opt Laser Technol* 152:108129. <https://doi.org/10.1016/j.optlastec.2022.108129>
3. Lü L, Fuh J, Wong YS (2001) *Laser-induced materials and processes for rapid prototyping*. Springer Sci Business Media. <https://doi.org/10.1007/978-1-4615-1469-5>
4. Huang AN, Kuo HP (2014) Developments in the tools for the investigation of mixing in particulate systems—a review. *Adv Powder Technol* 25(1):163–173. <https://doi.org/10.1016/j.apt.2013.10.007>
5. Xing X, Zhang C, Jiang B, Sun Y, Zhang L, Briens C (2022) Numerical study of the effect of the inlet gas distributor on the bubble distribution in a bubbling fluidized bed. *Chem Eng Res Des* 177:70–82. <https://doi.org/10.1016/j.cherd.2021.10.021>
6. Banaei M, Jegers J, van Sint AM, Kuipers JAM, Deen NG (2018) Tracking of particles using TFM in gas-solid fluidized beds. *Adv Powder Technol* 29(10):2538–2547. <https://doi.org/10.1016/j.apt.2018.07.007>
7. Hernández-Jiménez F, Sánchez-Prieto J, Cano-Pleite E, Soria-Verdugo A (2018) Lateral solids meso-mixing in pseudo-2D fluidized beds by means of TFM simulations. *Powder Technol* 334:183–191. <https://doi.org/10.1016/j.powtec.2018.04.061>. (Get rights and content)
8. Cho I, Yang C, Kwon H, Bang B, Jeong S, Lee U (2022) Numerical simulation method of a circulating fluidized bed reactor using a modified MP-PIC solver of OpenFOAM. *Powder Technol* 409:117815. <https://doi.org/10.1016/j.powtec.2022.117815>
9. Song Z, Li Q, Li F, Chen Y, Ullah A, Chen S, Wang W (2022) MP-PIC simulation of dilute-phase pneumatic conveying in a horizontal pipe. *Powder Technol* 410:117894. <https://doi.org/10.1016/j.powtec.2022.117894>
10. Zhang DM, Han L, Huang ZK (2022) A numerical approach for fluid-particle-structure interactions problem with CFD-DEM-CSD coupling method. *Comput Geotech* 152:105007. <https://doi.org/10.1016/j.compgeo.2022.105007>
11. Aziz H, Sansare S, Duran T, Gao Y, Chaudhuri B (2022) On the applicability of the coarse grained coupled CFD-DEM model to predict the heat transfer during the fluidized bed drying of pharmaceutical granules. *Pharm Res* 39(9):1991–2003. <https://doi.org/10.1007/s11095-022-03366-z>
12. Zhang H, Meng W (2022) Study on dust suppression of air curtain soft-sealing system of grab ship unloader. *Processes* 10(8):1505. <https://doi.org/10.3390/pr10081505>
13. Varas AC, Peters EAJF, Kuipers JAM (2017) CFD-DEM simulations and experimental validation of clustering phenomena and riser hydrodynamics. *Chem Eng Sci* 169:246–258. <https://doi.org/10.1016/j.ces.2016.08.030>
14. Peng X, Rao G, Li B, Wang S, Chen W (2020) Investigation on the gas–solid two-phase flow in the interaction between plane shock wave and quartz sand particles. *Appl Sci* 10(24):8859. <https://doi.org/10.3390/app10248859>
15. Kuruneru STW, Marechal E, Deligant M, Khelladi S, Ravelet F, Saha SC (2019) A comparative study of mixed resolved–unresolved CFD-DEM and unresolved CFD-DEM methods for the solution of particle-laden liquid flows. *Arch Comput Methods Eng* 26:1239–1254. <https://doi.org/10.1007/s11831-018-9282-3>
16. Cleary PW (2013) Particulate mixing in a plough share mixer using DEM with realistic shaped particles. *Powder Technol* 248:103–120. <https://doi.org/10.1016/j.powtec.2013.06.010>
17. Wang S, Shen Y (2022) Coarse-grained CFD-DEM modelling of dense gas-solid reacting flow. *Int J Heat Mass Transf* 184:122302. <https://doi.org/10.1016/j.ijheatmasstransfer.2021.122302>
18. Yan H, Huang Z, Hu M, Qi J, Liu L (2022) Numerical modeling of gas-solid two-phase flow in a plasma melting furnace. *Powder Technol* 412:117967. <https://doi.org/10.1016/j.powtec.2022.117967>

19. Shih TH, Liou W, Shabbir A, Yang Z, Zhu J (1995) A new k- ϵ eddy viscosity model for high reynolds number turbulent flows. *Comput Fluids* 24(3):227–238. [https://doi.org/10.1016/0045-7930\(94\)00032-T](https://doi.org/10.1016/0045-7930(94)00032-T)
20. Wang L, Zhang J, Zha X (2022) CFD-DEM study on mixing characteristics of ZrO₂ particles using the fluidized bed-chemical vapor deposition method. *Mater Today Commun* 33:104595. <https://doi.org/10.1016/j.mtcomm.2022.104595>
21. Hu P, Wang LX, Guo LM (2014) Analysis of an airdrop motion coupling NS equations with 6 DOF motion equations. *Adv Mater Res* 1016:506–510. <https://doi.org/10.4028/www.scientific.net/amr.1016.506>
22. Murakami S, Mochida A (1989) Three-dimensional numerical simulation of turbulent flow around buildings using the k- ϵ turbulence model. *Build Environ* 24(1):51–64. [https://doi.org/10.1016/0360-1323\(89\)90016-4](https://doi.org/10.1016/0360-1323(89)90016-4)

Publisher's Note Springer Nature remains neutral with regard to jurisdictional claims in published maps and institutional affiliations.

Springer Nature or its licensor (e.g. a society or other partner) holds exclusive rights to this article under a publishing agreement with the author(s) or other rightsholder(s); author self-archiving of the accepted manuscript version of this article is solely governed by the terms of such publishing agreement and applicable law.